NANO LETTERS

Letter

pubs.acs.org/NanoLett

Insight into the Capacity Fading Mechanism of Amorphous Se_2S_5 Confined in Micro/Mesoporous Carbon Matrix in Ether-Based Electrolytes

Gui-Liang Xu,[†] Tianyuan Ma,[†,¶] Cheng-Jun Sun,[‡] Chao Luo,[§] Lei Cheng,[∥] Yang Ren,[‡] Steve M. Heald,[‡] Chunsheng Wang,[§] Larry Curtiss,[∥] Jianguo Wen,[⊥] Dean J. Miller,[⊥] Tao Li,[‡] Xiaobing Zuo,[‡] Valeri Petkov,[#] Zonghai Chen,*[,†] and Khalil Amine*[,†]

[†]Chemical Sciences and Engineering Division, Argonne National Laboratory, Lemont, Illinois 60439, United States

[¶]Materials Science Program, University of Rochester, Rochester, New York 14627, United States

[‡]X-ray Science Division, Argonne National Laboratory, Lemont, Illinois 60439, United States

[§]Department of Chemical and Biomolecular Engineering, University of Maryland, College Park, Maryland 20742, United States

[∥]Materials Science Division, Argonne National Laboratory, Lemont, Illinois 60439, United States

[⊥]Center for Nanoscale Materials, Nanoscience Technology, Argonne National Laboratory, Lemont, Illinois 60439, United States

[#]Department of Physics, Central Michigan University, Mt. Pleasant, Michigan 48859, United States

S *Supporting Information*

ABSTRACT: In contrast to the stable cycle performance of space confined Se-based cathodes for lithium batteries in carbonate-based electrolytes, their common capacity fading in ether-based electrolytes has been paid less attention and not yet well-addressed so far. In this work, the lithiation/delithiation of amorphous Se_2S_5 confined in micro/mesoporous carbon (Se_2S_5/MPC) cathode was investigated by in situ X-ray near edge absorption spectroscopy (XANES) and theoretical calculations. The Se_2S_5/MPC composite was synthesized by a modified vaporization−condensation method to ensure a good encapsulation of Se_2S_5 into the pores of MPC host. In situ XANES results illustrated that the lithiation/delithiation reversibility of Se component was gradually decreased in ether-based electrolytes, leading to an aggravated formation of long-chain polyselenides during cycling and further capacity decay. Moreover, ab initio calculations revealed that the binding energy of polyselenides (Li_2Se_n) with carbon host is in an order of Li_2Se_6 > Li_2Se_4 > Li_2Se. The insights into the failure mechanism of Se-based cathode gain in this work are expected to serve as a guide for future design on high performance Se-based cathodes.

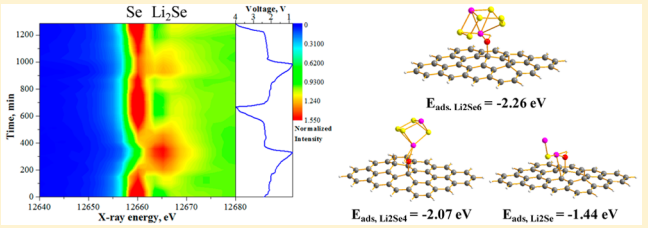

KEYWORDS: *Se_2S_5/MPC cathode, batteries, capacity fading, ether-based electrolytes, in situ XANES, ab initio calculations*

Lithium/sulfur (Li/S) batteries have been under scrutiny in the past decades owing to its low cost, abundance, and nontoxicity as well as much higher energy density than conventional lithium ion battery.[1,2] Lithium/selenium (Li/Se) batteries have also attracted an increasing attention in recent years owing to its comparable volumetric capacity with sulfur and much higher electronic conductivity (~20×) than sulfur.[3] A new concept based on selenium−sulfur composites by combining the advantage of sulfur and selenium was previously developed by our group, which can be used as cathode for both lithium and room temperature sodium batteries.[4] However, the electrochemical performances of these selenium-based cathodes in terms of reversible capacity, cycle stability, and rate capability still need optimization. It has been intensively reported that the electrolytes play a great role on the electrochemical performance of sulfur and selenium based cathodes.[5,6] Among them, carbonate-based and ether-based electrolytes are two kinds of popular electrolytes for selenium−sulfur based cathodes. Selenium has been found to be well-adaptive to carbonate-based electrolytes, while sulfur does not. The space-confined selenium displays excellent electrochemical performance in Li−Se batteries with carbonate-based electrolytes.[7] Meanwhile, even well-confined in the carbon host materials, most sulfur cathodes does not work well in carbonate-based electrolytes with very few exceptions, such as when confined in small micropores (pore size <0.5 nm), which is due to the nucleophilic attack to the carbonyl groups.[8,9] Recently, amorphous sulfur-rich $S_{1-x}Se_x$/C ($x \leq 0.1$) composite was reported by Li et al., which was prepared by immobilizing sulfur in the porous carbon via the interaction of a small amount of

Received: January 25, 2016
Revised: March 2, 2016
Published: March 29, 2016

DOI: 10.1021/acs.nanolett.6b00318
Nano Lett. 2016, 16, 2663−2673

selenium and demonstrated excellent electrochemical performance in carbonate-based electrolytes.[10]

It was reported that ether-based electrolytes could facilitate the redox reaction of sulfur-based cathodes and generally offer higher reversible capacity than that of carbonate-based electrolytes.[11] However, compared to Se-based cathodes in carbonate-based electrolytes,[12−15] researches focused on ether-based electrolytes are barely reported until a recent breakthrough reported by Cui et al.[7] They performed an in-depth study on the first lithiation/delithiation process of Se-based cathodes in ether-based electrolytes by synchrotron X-ray diffraction and X-ray absorption near edge spectroscopy (XANES). It was found that Se is reduced to the polyselenides, Li_2Se_n ($n \geq 4$), Li_2Se_2, and Li_2Se sequentially during the lithiation process, and Li_2Se is oxidized to Se through Li_2Se_n ($n \geq 4$) during the delithiation process in the first cycle, which undergoes similar reaction process to the sulfur system. Therefore, it is very important to design rational Se cathodes with conductive host to constrain the polyselenides and avoid the shuttle effect. Lots of carbonaceous materials with different pore structures, specific surface area, and morphology such as 3D interconnected hierarchical porous carbon aerogels,[16] nitrogen-containing hierarchical porous carbon,[17] 3D mesoporous carbon/graphene hierarchical architecture,[18] polypyrrole hollow spheres,[19] hollow carbonized polyaniline spheres,[20] mesoporous carbon microspheres,[21] reduced graphene oxide,[22] MWCNTS,[23] mesoporous aerogels,[24] and bimodal porous carbon[25] were then investigated for Se-based cathodes in ether-based electrolytes. However, it was found that, even with a very good encapsulation of selenium or selenium−sulfur in the various carbon host materials, most of the previous reported Se-based cathodes still show a gradual capacity fading in ether-based electrolytes.[7,16−28] Meanwhile, it has been also widely reported that sulfur/carbon composites with sulfur loading ranging from 30 wt % to 75 wt % can generally maintain a stable reversible capacity above 600 mA h g^{-1} within 100 cycles in ether-based electrolytes by optimizing the structure of carbon host materials.[11,29−35] Therefore, the confinement of carbon host for polysulfides and polyselenides should be different as they both suffer from dissolution in ether-based electrolytes. To the best of our knowledge, such a ubiquitous phenomenon has been paid less attention and not yet well addressed. Moreover, the detailed capacity fading mechanism of Se-based cathodes in ether-based electrolytes is still unknown.

Understanding the lithiation/delithiation process of battery materials is crucial for the successful development of high performance lithium batteries. However, lithium batteries are a very complex system, which involves liquid and solid, as well as amorphous and crystalline phases. Unlike X-ray diffraction that is limited to crystalline samples, X-ray absorption spectroscopy especially XANES is sensitive to the electronic changes and/or oxidation state of all the atoms of the targeted type in the samples. In this work, we are motivated to disclose the lithiation/delithiation process and capacity fading mechanism of Se-based cathodes in ether-based electrolytes upon continuous cycling by using in situ X-ray absorption near edge spectroscopy and ab initio calculations. Micro/mesoporous carbon (MPC) with a pore size about 2 nm was selected as carbon host to enhance the confinement for polysulfides and polyselenides. Se_2S_5/MPC composite with a Se_2S_5 loading of 50 wt % was then prepared by a modified vaporization-condensation method to ensure a good encapsulation of Se_2S_5 into the pores of MPC host. In situ XANES study reveals that the lithiation/delithiation reversibility of Se component was gradually decreased upon continuous cycling, leading to an aggravated formation of long-chain polyselenides during cycling and further capacity decay. Ab initio calculations further revealed that there is a pronounced preference on binding of long-chain polyselenides with carbon host than short-chain polyselenides. In addition, optimization on the cycle performance and rate capability of Se_2S_5/MPC cathode was discussed and carried out. The insights into the failure mechanism of Se-based cathode gain in this work are expected to serve as a guide for future design on high performance Se-based cathodes.

Experimental Section. *Preparation of Se_2S_5, Se_2S_5/MPC, and Se/MPC Composite.* All chemicals were purchased from Sigma-Aldrich and used without further treatment. Micro/mesoporous carbon (MPC) was received from our collaborator. The preparation of Se_2S_5/MPC composite was prepared by a modified vaporization−condensation method.[8,13,36] In a typical synthesis, sulfur powder, selenium powder, and MPC were mixed in a ratio of 1:1:2 by weight and then sealed in a glass tube under vacuum. The sealed glass tube was heated up to 600 °C with a heating rate of 5 °C min^{-1} in a box furnace and then held for 3 h before cooled down to room temperature naturally. Se_2S_5/MPC composite was finally collected as black powder. Bulk Se_2S_5 sample was also prepared similar to the preparation of Se_2S_5/MPC composite except without adding MPC. Se/MPC composite with a Se content of 50 wt % was prepared similar to the preparation of Se_2S_5/MPC composite except without adding sulfur.

Materials Characterization. The morphologies and structures of the as-synthesized materials were characterized by field emission scanning electron microscopy (HITACHI S-4700-II) and transmission electron microscopy (FEI Titan). Raman experiment was performed using a Renishaw inVia microscope spectrometer. The specific surface area and pore structure parameters of MPC were determined from the adsorption isotherm of nitrogen at 77K (NOVA-2020 Micromeritics Co., USA). The content of Se_2S_5 in the Se_2S_5/MPC composite was measured by thermo gravimetric analyses (TGA) on a STA 449 F3 instrument under argon atmosphere. Small angle X-ray scattering data were collected at Beamline 12-ID-B of APS. The 2D SAXS images were radically averaged to 1D profiles and presented in X-ray scattering intensities verse momentum transfer, q ($q = 4\pi \sin\theta/\lambda$, where θ is one-half of the scattering angle and $\lambda = 0.886$ Å is the wavelength of the X-ray at 12-ID-B), measured in the range of 0.01−2.3 $Å^{-1}$. High-energy synchrotron XRD experiments were carried out at the Beamline 11-ID-C at the Argonne National Laboratory using X-rays with wavelength of 0.11725 Å. During the measurements samples were sealed in glass capillaries and XRD data recorded with a large-area 2D detector up to wave vectors of 25 $Å^{-1}$. Diffraction data were reduced to atomic PDFs following well-established procedures.

Electrochemical Characterization. The slurry was prepared by spreading a mixture of 70 wt % active material, 20 wt % carbon black, and 10 wt % poly(acrylic acid) (9.8 wt %) onto a aluminum foil current collector. The as-prepared electrodes were then dried at 60 °C in a vacuum oven for 24 h. The loading density was controlled at 1.0−2.0 mg cm^{-2}. The electrochemical performances of the Se_2S_5/MPC electrodes were characterized by assembling them into coin cells (type CR2032) in an argon-filled glovebox under conditions that the content of moisture and oxygen were both below 0.5 ppm. The electrode was separated from lithium counter electrode by a

DOI: 10.1021/acs.nanolett.6b00318
Nano Lett. 2016, 16, 2663−2673

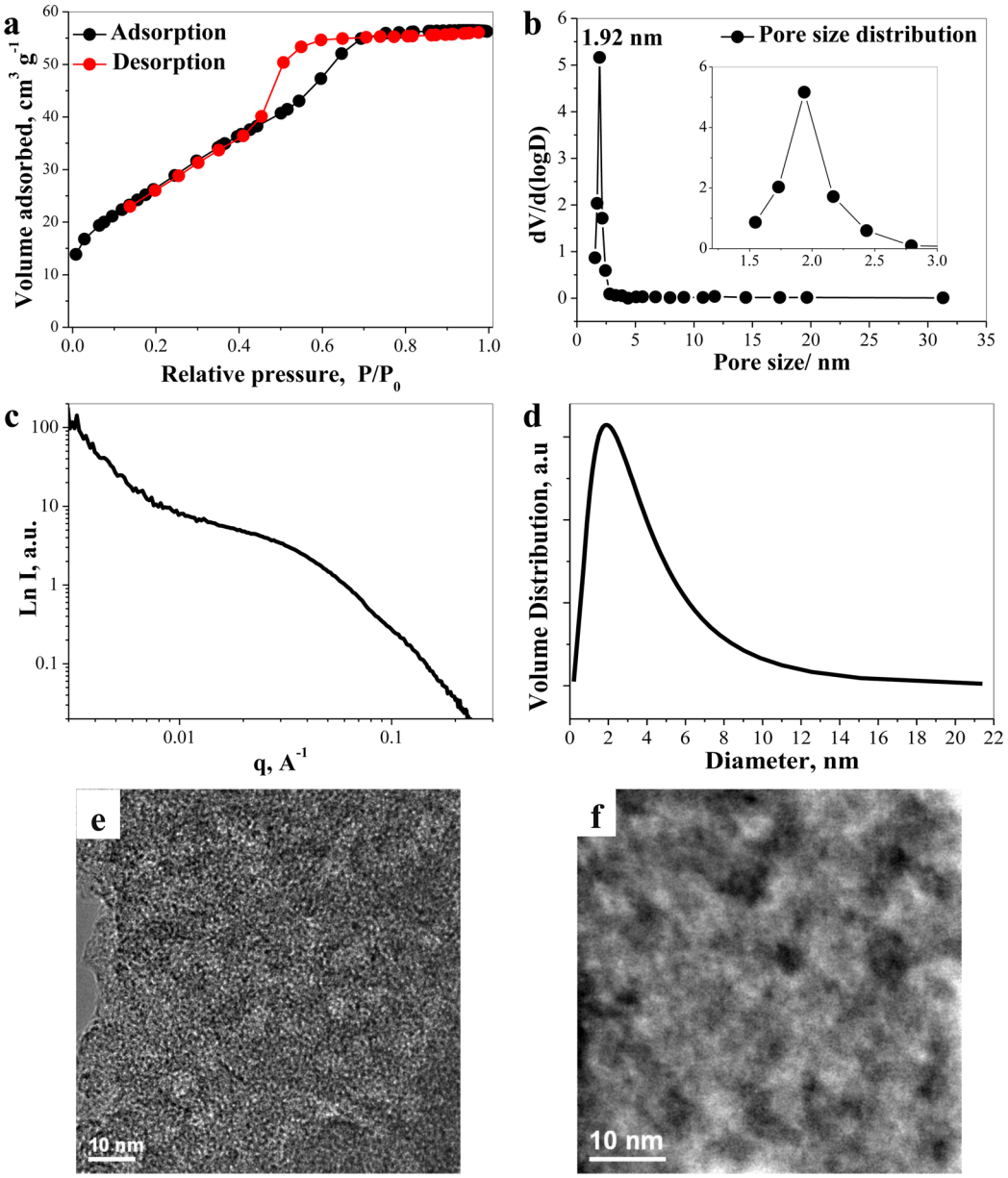

Figure 1. (a) N_2 adsorption−desorption isotherms curve and (b) pore size distribution and inset is the enlarged region between 1.5 and 3.0 nm, (c) SAXS and (d) pore size simulation, (e) bright-field TEM image, and (f) HAADF STEM image of MPC.

separator (Celgard 2325). Electrolyte used in the cell was 1.0 M lithium bis-trifluoromethanesulfonylimide (LiTFSI) in a mixture of 1,3-dioxolane (DOL) and dimethoxyethane (DME) (1:1 by volume) with 0.1 M $LiNO_3$ additive. The cells were charged and discharged using a MACCOR cycler. The capacties were calculated based on the active mass of Se_2S_5. Cyclic voltammogram of the Se_2S_5/MPC electrodes was recorded on a Solartron Analytical 1400 System between 0.8 and 4.0 V (vs Li/Li^+) at 0.1 mV s^{-1}.

In Situ X-ray Absorption Near Edge Spectroscopy. The in situ X-ray absorption near edge spectroscopy (XANES) experiments on Se K-edge between 12458 and 13458 keV was carried out in transmission mode at Beamline 20-BM-B of the APS. The incident beam was monochromatized by using a Si(111) fixed-exit, double-crystal monochromator.[7] During the in situ experiment, a MACCOR cycler was used to charged/discharged the cell using a constant rate of 0.2 C (1C = 1389 mA g^{-1}) between 0.8 and 4.0 V.

Computational Details. The ab initio calculations were performed using B3LYP/6-31+G* combination as implemented in Gaussian09 suite. The carbon substrate is an H-terminated graphene sheet with hydroxyl functional group as these groups are often present as defect on carbon surface and are likely the active binding sites for polyselenides. The binding energy (E_{bind}) of polyselenides on the carbon substrate is defined as $E_{bind} = E_{sub} + E_S - E_{sub+S}$ where E_{sub}, E_s, and E_{sub+S} represent the ground-state energies of the carbon substrate, polyselenides, and the corresponding polyselenides composite. A larger positive value refers to a greater binding ability.

Results and Discussion. Pore size of porous carbon materials is defined by the IUPAC as being either macro (>50 nm), meso (2−50 nm), or micro(<2 nm).[1] In order to enhance the confinement of carbon host for selenium−sulfur active materials, micro/mesoporous carbon (MPC) was used in this work. Nitrogen adsorption experiment was carried out to evaluate the specific surface area and the pore volume of the as-

DOI: 10.1021/acs.nanolett.6b00318
Nano Lett. 2016, 16, 2663−2673

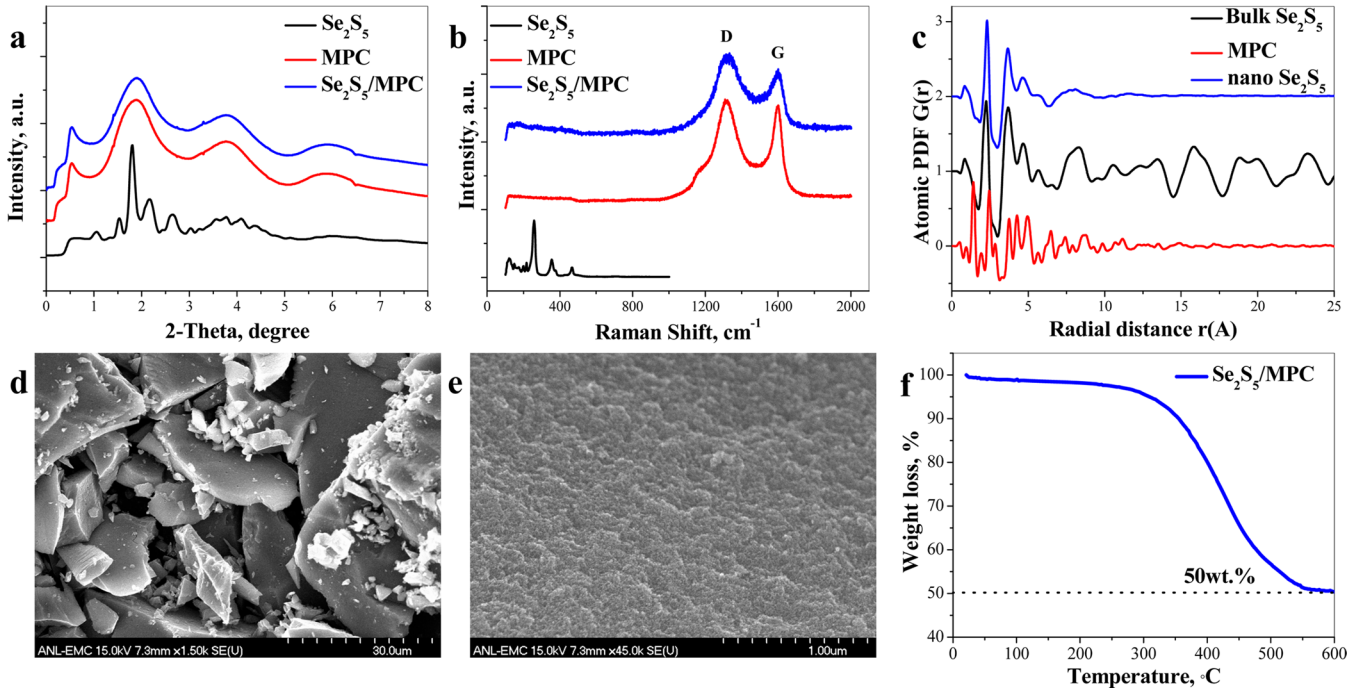

Figure 2. (a) HEXRD and (b) Raman of MPC, bulk Se_2S_5, and Se_2S_5/MPC; (c) PDF of MPC, bulk Se_2S_5, and nano Se_2S_5 that formed in the Se_2S_5/MPC; (d) low, (e) high magnification SEM images, and (f) TGA curve under argon atmosphere of Se_2S_5/MPC composite.

received MPC. Figure 1a shows the N_2 adsorption−desorption isotherms curve of MPC, which shows a typical type IV isotherm with a hysteresis loop, indicating the existence of well-developed porous structure. According to the Brunauer−Emmett−Teller (BET) model, the specific surface area of MPC is measured to be 848.8 $m^2\ g^{-1}$. For the pore size distribution, there is no obvious pore information from 3 to 32 nm. However, from the enlarged image inset, the MPC actually has a wide pore size range from 1.5 to 3 nm, which cover the range of microporous (<2 nm) and mesoporous (2−50 nm). The pore volume of MPC was 0.55 $cm^3\ g^{-1}$ as calculated by the Horváth-Kawazoe method (Figure 1b). The small-angle X-ray scattering (SAXS) spectrum of the MPC is shown in Figure 1c, which has a typical shape for cylindrical objects, having a diameter less than 100 nm. The average diameter of the MPC is approximately 2 nm by numerical analysis from the SAXS spectrum (Figure 1d), which is very close to that measured by BET. The microstructure of the MPC is further characterized by transmission electron microscopy (TEM). Figure 1e and f show bright-field TEM image and high-angle annular dark-field (HAADF) scanning TEM (STEM) image of MPC, respectively. Comparing to the bright-field TEM image, the *Z*-contrast HAADF image provides better information about micro/mesopores. In Figure 1f, lots of micropores with a size about 2 nm can be observed, in addition to few large mesopores with a size of about 4−5 nm. The pore size is similar to that characterized by BET and SAXS simulation. These micro/mesopores could be served as a good host for the infiltration of selenium−sulfur based active materials.

Se_2S_5/MPC composite was then prepared through a modified vaporization−condensation method to ensure a good encapsulation of Se_2S_5 into the micro/mesopores of MPC host. By this method, Se_2S_5 could be well-impregnated into the micro/mesopores of MPC.[8,37] The HEXRD patterns of bulk Se_2S_5, MPC, and Se_2S_5/MPC composite are compared in Figure 2a. The diffraction peaks at 0.5° that appeared in all three samples are attributed to the diffraction peak of the Kapton tube used for sample preparation. As shown, MPC presents three broad peaks due to its amorphous structure, while the bulk Se_2S_5 exhibits strong diffraction peaks owing to its large particle size. The Se_2S_5/MPC composite shows the same three broad peaks in the same 2-Theta position with MPC, indicating that Se_2S_5 particles may be either small or at an amorphous state. Similar to the HEXRD patterns, characteristic Raman peaks of Se_2S_5 are not observed in the Se_2S_5/MPC composite, and only two broad carbon peaks at 1327 and 1591 cm^{-1} representing the disordered graphite (D band) and crystalline graphite (G band), respectively, appear in the Raman spectrum of Se_2S_5/MPC composite (Figure 2b), suggesting that negligible amount of exterior Se_2S_5 exists in the Se_2S_5/MPC composites. The intensity ratio (I_D/I_G) of Se_2S_5/MPC between D band and G band has been slightly increased compared to MPC, which should be attributed to the infiltration of Se_2S_5 into the MPC host. The pair distribution function (PDF) provides local and long-range structural information as a histogram of all atom−atom distances within a system, independent of crystallinity.[38] Therefore, a PDF experiment was further conducted on the bulk Se_2S_5, MPC, and Se_2S_5/MPC to confirm their crystallinity (Figure 2c). It was found that the short-range structure of MPC is similar to graphite: the first three peaks are positioned at real space distances of 1.42, 2.46, and 2.83 Å, matching the in-plane carbon−carbon distances in graphite (1.43, 2.46, and 2.85 Å). The bulk Se_2S_5 is pretty crystalline, while the nano Se_2S_5 that formed in the Se_2S_5/MPC composite looks like inorganic glass. Noted that the PDF pattern of nano Se_2S_5 was obtained by subtraction between Se_2S_5/MPC and MPC. The PDF shape of nano Se_2S_5 resembles that of the PDF for bulk Se_2S_5, indicating that the nano Se_2S_5 has the same local atomic ordering structure of bulk Se_2S_5. A debate is about the formation of Se_2S_5 or a mixture of selenium and sulfur during the preparation of Se_2S_5 and Se_2S_5/MPC. The Raman spectra (Figure S1a) and

DOI: 10.1021/acs.nanolett.6b00318
Nano Lett. 2016, 16, 2663−2673

HEXRD pattern (Figure S1b) of sulfur, selenium, and bulk Se_2S_5 clearly show that the as-prepared Se_2S_5 is a new compound instead of a physical mixture of sulfur and selenium. The scanning electron microscopy (SEM) images of the Se_2S_5/MPC composite in Figure 2d and e shows that there are no large particles formed on the surface of MPC compared to the SEM image of pure MPC (Figure S1c). The thermogravimetric analysis (TGA) curve of the Se_2S_5/MPC composite under argon atmosphere shows a main weight loss at a temperature range of 300−550 °C, demonstrating that the content of Se_2S_5 in the composite was about 50 wt %, which is very close to the designed weight ratio (Figure 2f). The SEM X-ray energy dispersive spectroscopy (EDS) elemental mapping of Se_2S_5/MPC in Figure S2 clearly shows that carbon, sulfur, and selenium are uniformly distributed throughout the Se_2S_5/MPC composite, in agreement with the above HEXRD, Raman, and PDF analysis. To identify the microstructure further, bright-field TEM image and HAADF STEM image of the Se_2S_5/MPC composite were presented in Figure 3a and b. As shown, there

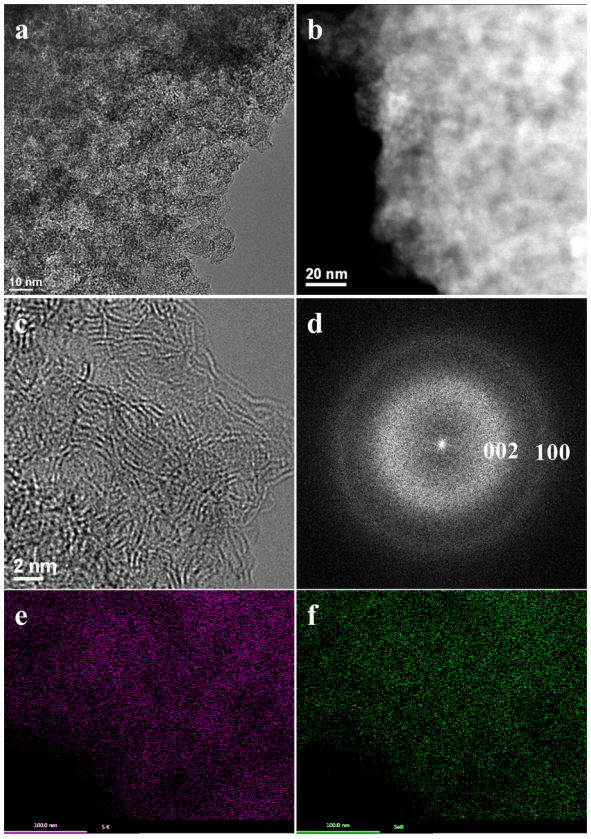

Figure 3. (a) Bright-field TEM image, (b) HAADF STEM image, (c) HRTEM image, and (d) the corresponding Fast Fourier Transform (FFT) pattern of the Se_2S_5/MPC composite. TEM elemental mapping images of (e) sulfur and (f) selenium in the Se_2S_5/MPC composite.

are no obvious morphology changes compared to that of MPC. In the HAADF image (Figure 3b), one can see many small brighter dots with a size of 1−2 nm, especially near the edge of sample due to less overlapping effect at thin areas. These bright dots correspond to high Z elements Se and S since the HAADF image is roughly proportional to Z^2.[39] High-resolution TEM image (Figure 3c) shows graphite lattices, but no lattice related to Se_2S_5 was found in the fast Fourier transform (FFT) pattern of Figure 3d, confirming that Se_2S_5 is in an amorphous state. The TEM elemental mapping images in Figure 3e and f further confirm the uniform distribution of sulfur and selenium in the Se_2S_5/MPC composite. In one word, the above finding indicates that Se_2S_5 is in an amorphous state and well-embedded into the micro/mesopores of MPC host materials, which presents similar structures to the previous reported Se/carbon nanocomposites.[24] The well encapsulated Se_2S_5 in the MPC host could help us identifying the common issue during cycling for Se-based cathodes in ether-based electrolytes.

In order to understand the lithiation/delithiation mechanism of Se_2S_5/MPC cathode, cyclic voltammogram (CV) of Se_2S_5/MPC cathode in ether-based electrolytes in the first five cycles was conducted at a scan rate of 0.1 mV s^{-1} within the voltage range of 0.8−4.0 V. As shown in Figure S3, the CV curves present four main reduction peaks and one main broad oxidation peak in the first cycle, which is consistent with the result reported by Abouimrane.[7] The weak reduction peak at 1.6 V and the oxidation peak at 3.5 V appeared in the first cycle and disappeared in the subsequent cycles may be due to the reduction and oxidation of $LiNO_3$ additive, which cannot be seen in the result reported by Abouimrane[7] as there are no $LiNO_3$ additives in their electrolytes. During the negative scan, the first reduction peak at around 2.29 V corresponds to the conversion of long-chain polysulfides to short-chain polysulfides. As the reduction proceeds, short-chain polysulfides were further converted to Li_2S_2 and/or Li_2S, which should be responsible for the third reduction peak at about 2.04 V.[24,29] The second reduction peak at around 2.12 V and the fourth reduction peak at around 1.77 V can be attributed to the conversion of Se component to polyselenides (Li_2Se_n, $n \geq 4$) and then to Li_2Se, respectively.[16−18,23] During the positive scan, only one oxidation peak at about 2.53 V is observed, which suggests that the "recovered" product after the charge may be intermediate S_8^{2-} and Se_8^{2-} instead of elemental S and Se.[7] However, the CV curves in the subsequent cycles are obviously different to that in the first cycle. In the discharge process, the intensities for the reduction peaks of Se component especially the peaks at about 1.77 V were obviously decreased, suggesting that the transformation of polyselenides (Li_2Se_n, $n \geq 4$) to Li_2Se was gradually decreased. The reduction peaks of sulfur component are more stable compared to Se component. In the oxidation process, the oxidation peak in the first cycle was split into four oxidation peaks. Compared to the gradually decreased peak intensities for the oxidation of Li_2Se, the peaks for the transformation of short-chain polysulfides to long-chain polysulfides are also more stable. Therefore, the CV results demonstrate that the reversibility for the lithiation/delithiation of Se component in the Se_2S_5/MPC composite is gradually decreased, which may be responsible for the common gradual capacity fading of Se-based cathodes in ether-based electrolytes.[16,17,19−28]

In order to gain further insights into the electrochemical behavior of Se_2S_5/MPC cathode in ether-based electrolytes, in situ X-ray absorption near edge spectroscopy (XANES) Se K-edge measurement on the Se_2S_5/MPC cathode during cycling was carried out as XANES is useful for determining the average chemical environment of the elements in all phases involves liquid and solid, as well as crystalline and/or amorphous phases.[40−42] The structure of the in situ electrochemical cell is shown in Figure S4, which used a typical coin cell with a hole for X-ray penetration. Figure 4a shows the 2D contour plot of in situ XANES data for the discharge and charge process of Se_2S_5/MPC cathode at 0.2 C (1C = 1389 mA g^{-1}) in the first

DOI: 10.1021/acs.nanolett.6b00318
Nano Lett. 2016, 16, 2663−2673

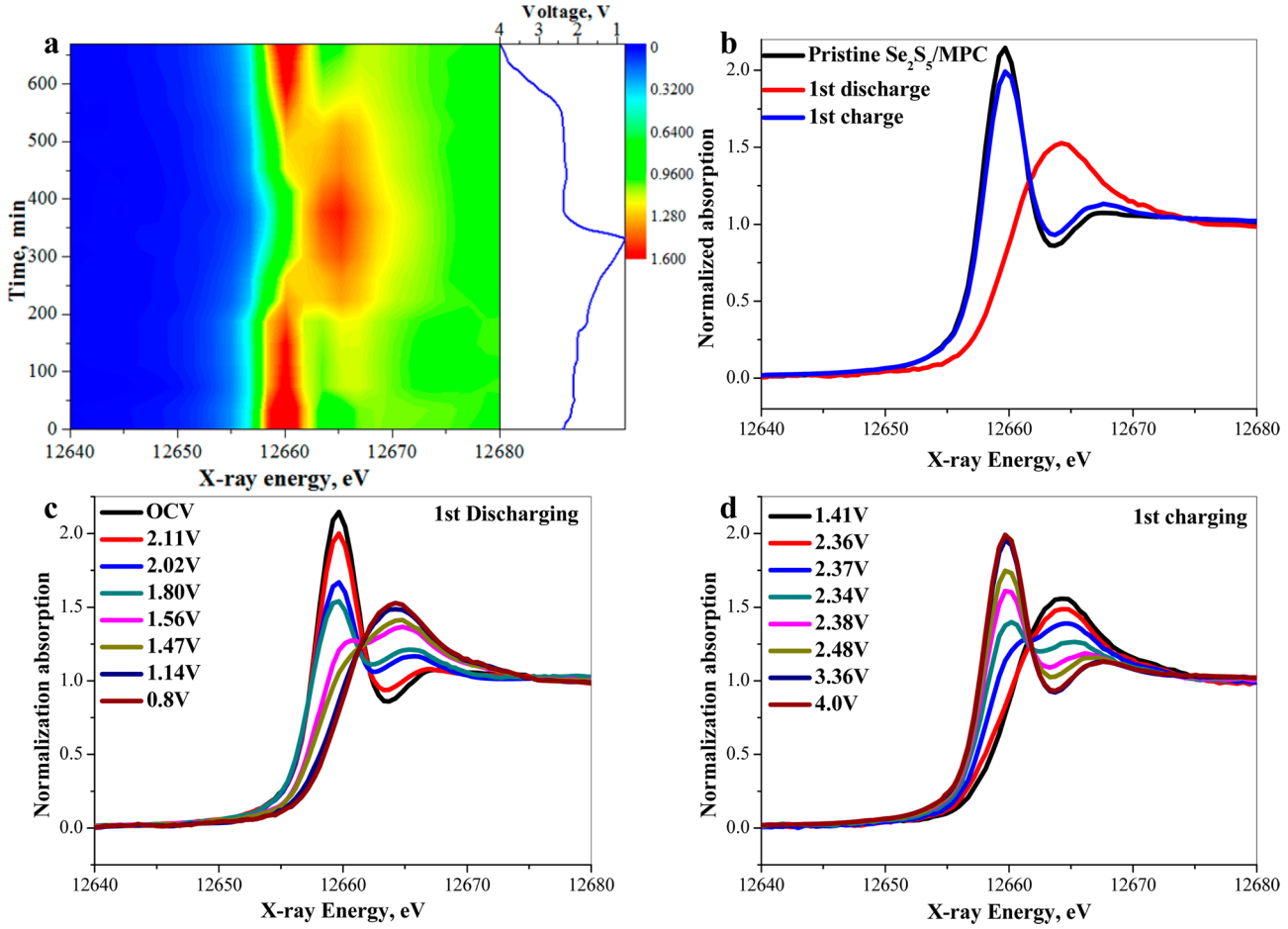

Figure 4. (a) 2D contour plot of in situ XANES data of Se_2S_5/MPC cathode at 0.2 C (1C = 1389 mA g^{-1}) for the first cycle, (b) typical Se K-edge XANES spectra for the pristine Se_2S_5/MPC, first discharge state and first charge state, typical Se K-edge XANES spectra collected at different potential during the first (c) discharge and (d) charge process of Se_2S_5/MPC cathode at 0.2 C (1C = 1389 mA g^{-1}).The color represents the normalized absorption intensity.

cycle. The color reflects the normalized absorption intensity, the red color represents high intensity, and the blue color means low intensity. In addition, the voltage profile in the first cycle is also displayed and correlated with the evolution of the XANES data. For example, the inflection point observed in the contour plot of the XANES data coincides well with the critical point in the fully discharge state. The apparent symmetry of the data set emphasizes that the discharging and charging proceed through a reversible sequence of reactions in the first cycle. The typical Se K-edge XANES spectra for the pristine Se_2S_5/MPC, first discharge state and first charge state are shown in Figure 4b. The Se K-edge absorption energy for pristine Se_2S_5/MPC matched well with that of Selenium powder (12658 eV), which is assigned to the transition of Se 1s core electrons to the unoccupied 4p state.[7] The spectrum for the electrode in the first discharged state is similar to that of Li_2Se, indicating the formation of Li_2Se phase when the cell was discharged to 0.8 V. The shift of Se K-edge to a higher energy from Se to Li_2Se may be due to the increasing oxidation state and/or reduced screening effect.[7] In order to further confirm the transformation of Se to Li_2Se, we have conducted ex situ high energy X-ray diffraction on the first discharged product. The pristine material presented no crystalline peaks due to the amorphous state of Se_2S_5 in the MPC (see Figure 2a). While in the HEXRD pattern of the first discharged electrode (Figure S5), in addition to the strong signal of Al current collector, we can also observe the diffraction peaks of Li_2S and Li_2Se, confirming the transformation of Se_2S_5 to Li_2S and Li_2Se during the lithiation process. When the cell was charged back to 4.0 V, the Se K-edge shifted back to lower energy for Se K-edge, suggesting that the Se could be almost recovered. In order to understand the detailed reaction along with the potential, in situ XANES spectra under different potential during discharge and charge process are depicted in Figure 4c and d, respectively. As shown, upon discharging, the absorption peaks belong to selenium have a relatively large decrease starting from about 2.11 V, while the signal for Li_2Se was gradually increased from about 1.80 V. During the first charge process, the spectra have little change until the voltage went to 2.37 V. After that, the signal of Li_2Se was continuously decreased, and the intensity for Se was increased accordingly. The potential for the lithiation/delithiation of Se component in the first cycle are quite consistent with that in the CV of Se_2S_5/MPC. In brief, in situ XANES study shows that the Se K-edge is shifted significantly with (de) lithiation in the first cycle and is in agreement with that reported by Cui and et al.[7]

Linear combination fitting included in the Athena software was commonly used to analyze the components for the intermediate products during electrochemical reaction. By selecting XANES spectra of the starting materials and discharge products as standards, the compositions of the intermediate products may be disclosed. Note that the intermediate products

DOI: 10.1021/acs.nanolett.6b00318
Nano Lett. 2016, 16, 2663−2673

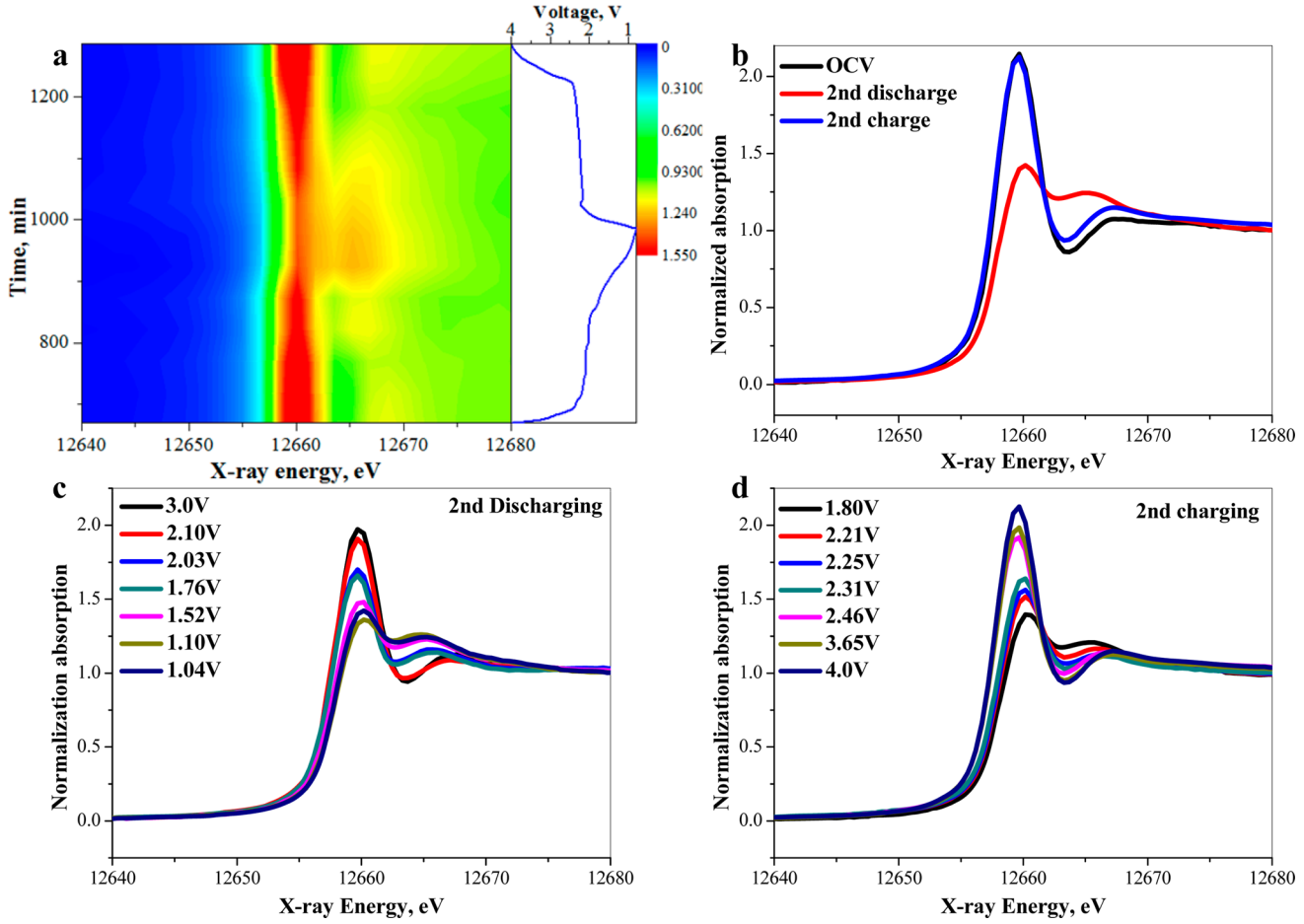

Figure 5. (a) 2D contour plot of in situ XANES data of Se_2S_5/MPC cathode at 0.2 C (1C = 1389 mA g^{-1}) for the second cycle, (b) typical Se K-edge XANES spectra for the pristine Se_2S_5/MPC, second discharge state and second charge state, typical Se K-edge XANES spectra collected at different potential during the second (c) discharge and (d) charge process of Se_2S_5/MPC cathode at 0.2 C (1C = 1389 mA g^{-1}). The color represents the normalized absorption intensity.

during electrochemical reaction should not be simple mixtures of Se and Li_2Se but actually a mixture of Se, Li_2Se_n and Li_2Se. For example, the fitting for the XANES spectrum collected at 1.80 V in the first discharge using two phases (Se and Li_2Se) and multiphases (Se, Li_2Se_n, and Li_2Se) are compared in Figure S6. As shown, the residual is much larger when using two phase fitting, while a better fitting was obtained using multiphase fitting. A quantitative analysis of the in situ data was not carried out because of the lack of standard spectrum; the spectrum collected at the end of discharge was used as a "pseudo" standard to illustrate the existence of an intermediate. However, it should reach a consensus that the evolution of selenium in ether-based electrolytes is from Se to Li_2Se through polyselenide intermediates.

Figure 5 shows in situ Se K-edge measurement data on the Se_2S_5/MPC cathode in ether-based electrolytes for the second cycle. The 2D contour plot for the second cycle in Figure 5a is significantly different from that of the first cycle. It can be seen that the reduction of Se component and formation of Li_2Se are not completed. Even at the end of the second discharge, the Se K-edge for Se and Li_2Se can be both observed. Figure 5b compares the typical Se K-edge XANES spectra for the pristine Se_2S_5/MPC, second discharge state, and second charge state. Although Se could be completely recovered at the end of the second charge, the XANES spectrum in the second discharge seems like a mixture of Se, polyselenides, and Li_2Se instead of sole Li_2Se. The XANES spectra under different potential during discharge in Figure 5c also reveal that the Se K-edge for Se has a little decrease from 2.10 to 2.03 V owing to the conversion of Se to long-chain polyselenides (Li_2Se_n, $n \geq 4$). However, when the cell was further discharged, the transformation of long-chain polyselenides (Li_2Se_n, $n \geq 4$) to Li_2Se that occurred in the first cycle was gradually decreased as indicated from the little change of the XANES spectra from 1.76 to 1.04 V. Figure 5d gives the XANES spectra collected during the second charge process. The result shows that all the polyselenides could be completely converted back to Se. Besides, the derivatives of the XANES data that can determine the energy position are shown in Figure S7. The results clearly demonstrate that the Se K-edge shifted from 12656.7 to 12660 eV and then shifted back to 12656.7 eV in the first cycle. However, the Se K-edge has little shift in the second cycle, further confirming that the lithiation/delithiation reversibility of Se component was decreased. To summary, in situ XANES study illustrates that the lithiation/delithiation reversibility of Se component in the Se_2S_5/MPC composite is gradually decreased upon continuous cycling even though the Se_2S_5 was well confined in the MPC host. This electrochemical characteristic will significantly affect its electrochemical performance in terms of reversible capacity, Coulombic efficiency and cycle performance as discussed below.

DOI: 10.1021/acs.nanolett.6b00318
Nano Lett. 2016, 16, 2663−2673

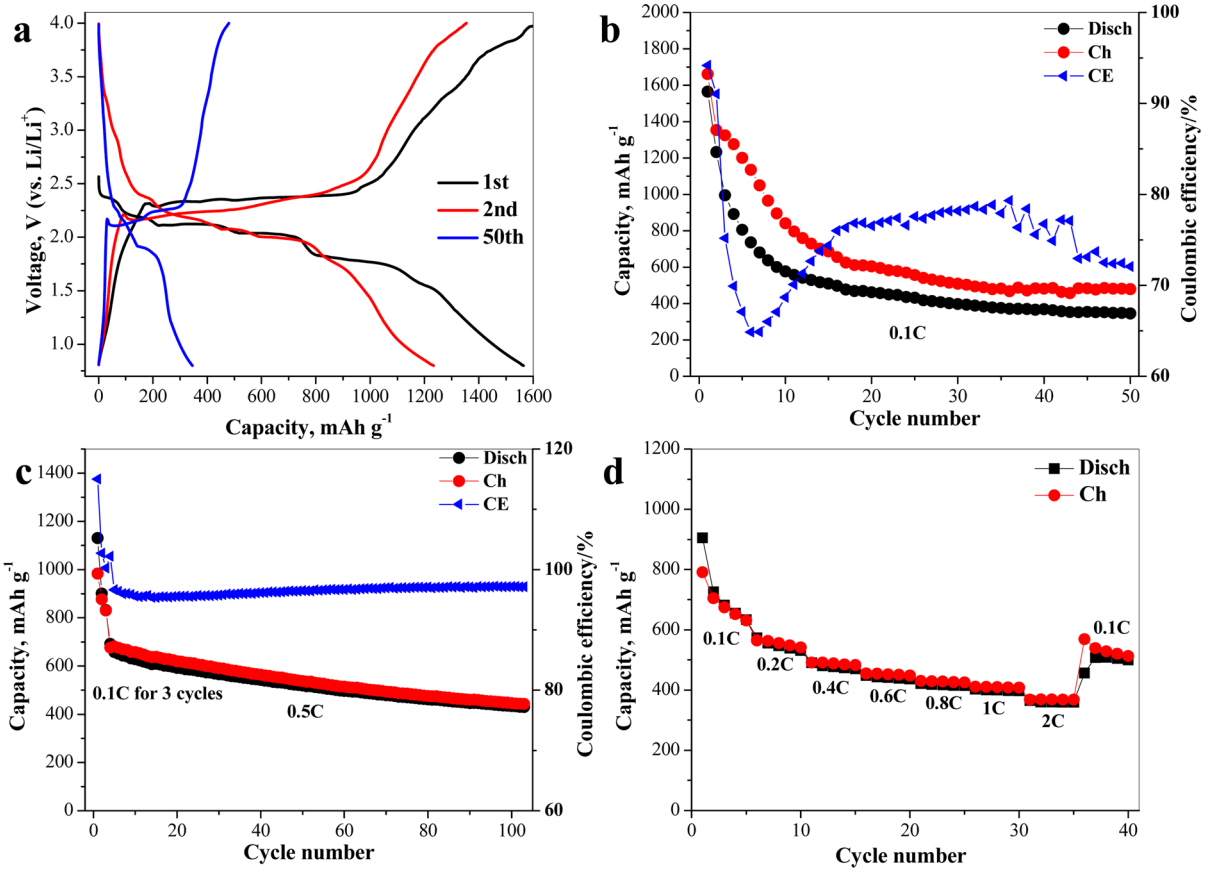

Figure 6. (a) Charge/discharge curves and (b) cycle performance of Se_2S_5/MPC composite at 0.1 C within 0.8−4.0 V. (c) Cycle performance at 0.5 C and (d) rate performance of Se_2S_5/MPC composite within 1.5−3.0 V.

The electrochemical performance of Se_2S_5/MPC cathode was evaluated by assembling them into coin cells with lithium as reference and counter electrode. The electrolytes are the widely studied ether-based electrolytes, 1.0 M lithium bis-trifluoromethanesulfonylimide in a mixture of 1,3-dioxolane (DOL) and dimethoxyethane (DME) (1:1 by volume) with 0.1 M $LiNO_3$ additive. The charge/discharge curves of Se_2S_5/MPC cathode in the first, second, and 50th cycle at 0.1 C (1C = 1389 mA g^{-1}) are shown in Figure 6a. Four main discharge plateaus at about 2.25, 2.03, 2.12, and 1.80 V are observed, representing the two-step lithiation process of sulfur and selenium, respectively. During its charge process, there is a long charge plateau ranging from 2.30 to 2.50 V, ascribing to the transformation of Li_2S and Li_2Se to long-chain polysulfides and polyselenides. These voltage plateaus coincide well with results from CV and in situ XANES. The first discharge capacity was measured to be 1564.6 mA h g^{-1}, slightly higher than the theoretical capacity of Se_2S_5 (1389 mA h g^{-1}). It is believed that this capacity includes the reduction of $LiNO_3$ additive in the first discharge process as indicated by the small discharge plateau (discharge curve) and the weak reduction peak (CV) at about 1.6 V.[29] The initial charge capacity is 1661.2 mA h g^{-1}, leading to a Coulombic efficiency of 94.1%. Figure 6b depicts the charge/discharge capacities and Coulombic efficiency along with increasing cycle number at 0.1 C. As shown, the Se_2S_5/MPC cathode presents a rapid capacity fading upon continuous cycling. After 50 cycles of charge/discharge, it can only maintain a discharge capacity of 345.5 mA h g^{-1}. Similar capacity fading tendency in ether-based electrolytes could be also observed in other previous reported Se-based cathodes.[16,17,19−27] Moreover, the Coulombic efficiency also gets very poor, indicating a severe shuttle effect. The cycle performance of Se/MPC composite was also investigated and shown in Figure S8. Its initial discharge/charge capacities were measured to be 481.1 mA h g^{-1} and 509.8 mA h g^{-1}, respectively. However, the capacity was significantly decreased in only 10 cycles, and a severe polyselenides shuttle was clearly observed, indicating that the rapid capacity fading and the low Coulombic efficiency of the Se_2S_5/MPC composite should come from the Se components. As discussed in the CV and in situ XANES study, an aggravated formation of long-chain polyselenides during cycling could be expected. The more formation of long-chain polyselenides, the lower specific capacity it will be as less electron transfer is involved. These polyselenides may further diffuse to the anode side and react with lithium to form short chain polyselenides and then oxidized to long-chain polyselenides again during the charge process, which will lead to polyselenides shuttle and corrosion of lithium anode as well as increase of internal resistance, and further the poor Coulombic efficiency and gradual capacity fading.[30]

To elucidate the mechanism of polyselenide detachment, we performed ab initio calculations to understand the surface interaction of polyselenides with a carbon surface. Different polyselenides, Li_2Se_n (n = 1, 4, 6), were investigated to compare their bonding strength with carbon host, while the carbon substrate is an H-terminated graphene sheet with hydroxyl functional group as these groups are often present as defect on carbon surface and are likely the active binding sites for polyselenides. The approach may not give an absolute

DOI: 10.1021/acs.nanolett.6b00318
Nano Lett. 2016, 16, 2663−2673

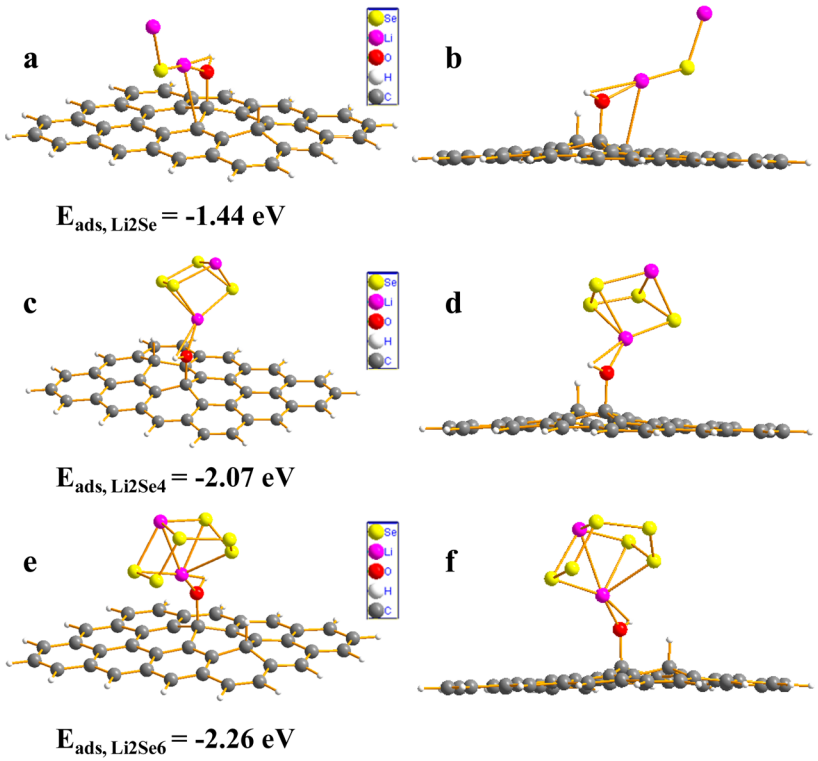

Figure 7. Ab initio calculations on the binding energy of different polyselenides with carbon host: (a, b) Li_2Se, (c, d) Li_2Se_4, (e, f) Li_2Se_6.

quantification of the binding strength between the polyselenides with the carbon surface but will provide a good comparison with different polyselenides and hence the interfacial effect on the cycling performance. The most stable geometric configurations of the different polyselenides with H-terminated graphene sheet with hydroxyl functional group are shown in Figure 7 with their binding energy values, respectively. As clearly shown, the binding energy is in an order of Li_2Se_6 (−2.26 eV) > Li_2Se_4 (−2.07 eV) > Li_2Se (−1.44 eV), indicating that there is a favorable bonding between long-chain polyselenides with carbon surface. CV and in situ XANES study found that the transformation of long-chain polyselenides to short-chain polyselenides was suppressed during cycling, which may be due to the weaker binding energy of short-chain polyselenides with carbon surface than long-chain polyselenides. Therefore, an aggravated formation of long-chain polyselenides could be expected, which will lead to the gradual capacity fading during cycling. On the contrary, the binding strength of short-chain polysulfides with carbon host was found to be generally stronger than long-chain polysulfides, which may lead to the distinct cycle performance between sulfur cathodes and Se-based cathodes in ether-based electrolytes.[43,44] In addition, we have summarized recently reported works about Se-based cathodes using ether-based electrolytes as possible as we can. As shown in Table S1, it all shows poor cycle performance although most of the Se and Se−S are also well-embedded into the corresponding carbon host. Considering in situ XANES results and the ab initio calculations together with the related works reported in the current literatures, we concluded that the current DOL-DME based electrolytes may be not a good electrolyte for space-confined Se-based cathodes as the lithiation/delithiation reversibility was gradually decreased upon continuous cycling, while carbonate-based electrolytes may be a better choice as the excellent electrochemical performance of the well-confined Se-based cathodes in carbonate-based electrolytes have been widely reported.[8,13−15,36,45−47]

Given that space-confined sulfur cathodes can work in carbonate-based electrolytes by subnano confinement, Se-based cathodes may also work in ether-based electrolytes in some restriction. As recently reported by Han et al., although Se/mesoporous carbon (Se/MCN) particles illustrated rapid capacity fading in ether-based electrolytes, the RGO coating indeed greatly increased the reversible capacity and the cycle stability of Se/MCN composite.[18] The cycle life of Se-based cathode could be also improved by using a graphene-coated separator, which can localize the highly soluble polyselenides in the separator and prevent its further reaction with lithium metal.[48] In addition to the surface coating and separator optimization, more factors are discussed in this work. It is well-known that the depth of discharge (DOD) and state of charge (SOC) could greatly affect the cycle life of battery. Therefore, the cycle performance and rate capability of the Se_2S_5/MPC composite in a voltage range of 1.5−3.0 V instead of 0.8−4.0 V were evaluated. The cell was first cycled at 0.1 C for 3 cycles and then cycled at 0.5 C for the subsequent cycles. As shown in Figure 6c, the Se_2S_5/MPC composite could deliver a discharge capacity of 691.9 mA h g^{-1} at 0.5 C for the first cycle. After 100 cycles of charge/discharge at 0.5 C, it can still maintain a capacity of 430.2 mA h g^{-1}, illustrating higher reversible capacity and better cycle stability than that within the voltage range of 0.8−4.0 V. Moreover, the Coulombic efficiency is also improved. Except the first cycle, the Coulombic efficiency stabilized at about 100% in the subsequent cycles, suggesting a suppressed shuttle effect. The rate capability of the Se_2S_5/MPC composite was also tested to investigate its fast charge/discharge performance. The charge/discharge rates were successively increased from 0.1 C, 0.2 C, 0.4 C, 0.6 C, 0.8 C,

DOI: 10.1021/acs.nanolett.6b00318
Nano Lett. 2016, 16, 2663−2673

1 to 2 C, and then decreased back to 0.1C again. As shown in Figure 6d, the reversible capacity was gradually decreased along with increasing the rate. However, at a high rate of 2 C, it can still deliver a capacity of about 360 mA h g^{-1}. When we decreased the rate back to 0.1 C, an average capacity of about 500 mA h g^{-1} could be recovered. In a word, ether-based electrolytes could facilitate the redox reaction of Se-based cathode but also bring challenges. In order to make Se-based cathodes work well in ether-based electrolytes, surface modification, separator optimization, DOD/SOC optimization and other efforts such as electrolytes and binder optimization may be done.

Conclusions. In this work, the capacity fading mechanism of space confined Se-based cathode in ether-based electrolytes upon continuous cycling was investigated by in situ XANES technique and theoretical calculations. The Se_2S_5/MPC composite was prepared by a modified vaporization−condensation method to ensure a good encapsulation of Se_2S_5 into the MPC host. The HEXRD, Raman, PDF, SEM, and TEM showed that the Se_2S_5 are well-embedded into the micro/mesopores of MPC and existed in an amorphous state. In situ XANES results demonstrated that the lithiation/delithiation reversibility of Se component was gradually decreased in ether-based electrolytes, leading to an aggravated formation of long-chain polyselenides upon continuous cycling. Ab initio calculations further revealed that there is a pronounced preference on binding of long-chain polyselenides with carbon host than short-chain polyselenides. We expect our current study could enable a better understanding on the lithiation/delithiation process of Se-based cathodes and facilitate the development of high performance Se-based cathodes in the future.

■ ASSOCIATED CONTENT

Supporting Information

The Supporting Information is available free of charge on the ACS Publications website at DOI: 10.1021/acs.nanolett.6b00318.

XRD, Raman, SEM of sulfur, selenium, and bulk Se_2S_5. SEM elemental mapping and cyclic voltammogram of Se_2S_5/MPC. Scheme for the in situ XANES cell. Linear combination fitting of the XANES spectrum collected at 1.80 V. Derivative of normalized XANES data of Se_2S_5MPC cathode. Cycle performance of Se/MPC composite at 0.1 C in ether-based electrolytes. Table for summary of Se-based cathodes in ether-based electrolytes (PDF)

■ AUTHOR INFORMATION

Corresponding Authors

*E-mail: zonghai.chen@anl.gov (Z.C.).
*E-mail: amine@anl.gov (K.A.).

Notes

The authors declare no competing financial interest.

■ ACKNOWLEDGMENTS

Research at the Argonne National Laboratory was funded by U.S. Department of Energy, Vehicle Technologies Office. Support from Tien Duong of the U.S. DOE's Office of Vehicle Technologies Program is gratefully acknowledged. Use of the Advanced Photon Source, an Office of Science User Facility operated for the U.S. Department of Energy (DOE) Office of Science by Argonne National Laboratory, was supported by the U.S. DOE under Contract No. DE-AC02-06CH11357. Sector 20 facilities at the Advanced Photon Source, and research at these facilities, are supported by the US Department of Energy Basic Energy Sciences, the Canadian Light Source and its funding partners, the University of Washington, and the Advanced Photon Source. This work was partially supported by DOE-BES grant DE-SC0006877 (V.P.).

■ REFERENCES

(1) Evers, S.; Nazar, L. F. *Acc. Chem. Res.* **2013**, *46*, 1135−1143.
(2) Ji, X. L.; Lee, K. T.; Nazar, L. F. *Nat. Mater.* **2009**, *8*, 500−506.
(3) Yang, C. P.; Yin, Y. X.; Guo, Y. G. *J. Phys. Chem. Lett.* **2015**, *6*, 256−266.
(4) Abouimrane, A.; Dambournet, D.; Chapman, K. W.; Chupas, P. J.; Weng, W.; Amine, K. *J. Am. Chem. Soc.* **2012**, *134*, 4505−4508.
(5) Cui, Y. J.; Abouimrane, A.; Sun, C. J.; Ren, Y.; Amine, K. *Chem. Commun.* **2014**, *50*, 5576−5579.
(6) Cui, Y.; Abouimrane, A.; Lu, J.; Bolin, T.; Ren, Y.; Weng, W.; Sun, C.; Maroni, V. A.; Heald, S. M.; Amine, K. *J. Am. Chem. Soc.* **2013**, *135*, 8047−8056.
(7) Luo, C.; Xu, Y.; Zhu, Y.; Liu, Y.; Zheng, S.; Liu, Y.; Langrock, A.; Wang, C. *ACS Nano* **2013**, *7*, 8003−8010.
(8) Xin, S.; Gu, L.; Zhao, N. H.; Yin, Y. X.; Zhou, L. J.; Guo, Y. G.; Wan, L. J. *J. Am. Chem. Soc.* **2012**, *134*, 18510−18513.
(9) Xu, Y. H.; Wen, Y.; Zhu, Y. J.; Gaskell, K.; Cychosz, K. A.; Eichhorn, B.; Xu, K.; Wang, C. S. *Adv. Funct. Mater.* **2015**, *25*, 4312−4320.
(10) Li, X. N.; Liang, J. W.; Zhang, K. L.; Hou, Z. G.; Zhang, W. Q.; Zhu, Y. C.; Qian, Y. T. *Energy Environ. Sci.* **2015**, *8*, 3181−3186.
(11) Manthiram, A.; Fu, Y.; Chung, S. H.; Zu, C.; Su, Y. S. *Chem. Rev.* **2014**, *114*, 11751−87.
(12) Zeng, L.; Zeng, W.; Jiang, Y.; Wei, X.; Li, W.; Yang, C.; Zhu, Y.; Yu, Y. *Adv. Energy Mater.* **2015**, *5*, 1401377.
(13) Luo, C.; Zhu, Y.; Wen, Y.; Wang, J.; Wang, C. *Adv. Funct. Mater.* **2014**, *24*, 4082−4089.
(14) Yang, C. P.; Xin, S.; Yin, Y. X.; Ye, H.; Zhang, J.; Guo, Y. G. *Angew. Chem., Int. Ed.* **2013**, *52*, 8363−8367.
(15) Ye, H.; Yin, Y. X.; Zhang, S. F.; Guo, Y. G. *J. Mater. Chem. A* **2014**, *2*, 13293−13298.
(16) Jiang, S. F.; Zhang, Z. A.; Lai, Y. Q.; Qu, Y. H.; Wang, X. W.; Li, J. *J. Power Sources* **2014**, *267*, 394−404.
(17) Qu, Y. H.; Zhang, Z. A.; Jiang, S. F.; Wang, X. W.; Lai, Y. Q.; Liu, Y. X.; Li, J. *J. Mater. Chem. A* **2014**, *2*, 12255−12261.
(18) Han, K.; Liu, Z.; Shen, J.; Lin, Y.; Dai, F.; Ye, H. *Adv. Funct. Mater.* **2015**, *25*, 455−463.
(19) Guo, J.; Wen, Z.; Ma, G.; Jin, J.; Wang, W.; Liu, Y. *RSC Adv.* **2015**, *5*, 20346−20350.
(20) Li, J.; Zhao, X. X.; Zhang, Z. A.; Lai, Y. Q. *J. Alloys Compd.* **2015**, *619*, 794−799.
(21) Liu, L.; Wei, Y.; Zhang, C.; Zhang, C.; Li, X.; Wang, J.; Ling, L.; Qiao, W.; Long, D. *Electrochim. Acta* **2015**, *153*, 140−148.
(22) Peng, X.; Wang, L.; Zhang, X. M.; Gao, B.; Fu, J. J.; Xiao, S.; Huo, K. F.; Chu, P. K. *J. Power Sources* **2015**, *288*, 214−220.
(23) Wang, X. W.; Zhang, Z. A.; Qu, Y. H.; Wang, G. C.; Lai, Y. Q.; Li, J. *J. Power Sources* **2015**, *287*, 247−252.
(24) Zhang, Z. A.; Jiang, S. F.; Lai, Y. Q.; Li, J. M.; Song, J. X.; Li, J. *J. Power Sources* **2015**, *284*, 95−102.
(25) Qu, Y.; Zhang, Z.; Lai, Y.; Liu, Y.; Li, J. *Solid State Ionics* **2015**, *274*, 71−76.
(26) Zhang, Z. A.; Yang, X.; Wang, X. W.; Li, Q.; Zhang, Z. Y. *Solid State Ionics* **2014**, *260*, 101−106.
(27) Zhang, Z. A.; Yang, X.; Guo, Z. P.; Qu, Y. H.; Li, J.; Lai, Y. Q. *J. Power Sources* **2015**, *279*, 88−93.
(28) Lee, J. T.; Kim, H.; Oschatz, M.; Lee, D. C.; Wu, F. X.; Lin, H. T.; Zdyrko, B.; Cho, W.; Kaskel, S.; Yushin, G. *Adv. Energy Mater.* **2015**, *5*, 1400981.

DOI: 10.1021/acs.nanolett.6b00318
Nano Lett. 2016, 16, 2663−2673

(29) Xu, G. L.; Xu, Y. F.; Fang, J. C.; Peng, X. X.; Fu, F.; Huang, L.; Li, J. T.; Sun, S. G. *ACS Appl. Mater. Interfaces* **2013**, *5*, 10782−10793.
(30) Chen, S. R.; Zhai, Y. P.; Xu, G. L.; Jiang, Y. X.; Zhao, D. Y.; Li, J. T.; Huang, L.; Sun, S. G. *Electrochim. Acta* **2011**, *56*, 9549−9555.
(31) Xu, G. L.; Wang, Q.; Fang, J. C.; Xu, Y. F.; Huang, L.; Sun, S. G. *J. Mater. Chem. A* **2014**, *2*, 19941−19962.
(32) Wang, Y. X.; Huang, L.; Sun, L. C.; Xie, S. Y.; Xu, G. L.; Chen, S. R.; Xu, Y. F.; Li, J. T.; Chou, S. L.; Dou, S. X.; Sun, S. G. *J. Mater. Chem.* **2012**, *22*, 4744−4750.
(33) Manthiram, A.; Fu, Y. Z.; Su, Y. S. *Acc. Chem. Res.* **2012**, *46*, 1125−1134.
(34) Yang, Y.; Zheng, G.; Cui, Y. *Chem. Soc. Rev.* **2013**, *42*, 3018−3032.
(35) Sun, H.; Xu, G. L.; Xu, Y. F.; Sun, S. G.; Zhang, X. F.; Qiu, Y. C.; Yang, S. H. *Nano Res.* **2012**, *5*, 726−738.
(36) Luo, C.; Wang, J.; Suo, L.; Mao, J.; Fan, X.; Wang, C. *J. Mater. Chem. A* **2015**, *3*, 555−561.
(37) Guo, J. C.; Xu, Y. H.; Wang, C. S. *Nano Lett.* **2011**, *11*, 4288−4294.
(38) Liu, B.; Abouimrane, A.; Balasubramanian, M.; Ren, Y.; Amine, K. *J. Phys. Chem. C* **2014**, *118*, 3960−3967.
(39) Pennycook, S. J. *Ultramicroscopy* **1989**, *30*, 58−69.
(40) Piao, Y.; Qin, Y.; Ren, Y.; Heald, S. M.; Sun, C. J.; Zhou, D. H.; Polzin, B. J.; Trask, S. E.; Amine, K.; Wei, Y. J.; Chen, G.; Bloom, I.; Chen, Z. H. *Phys. Chem. Chem. Phys.* **2014**, *16*, 3254−3260.
(41) Lv, D.; Bai, J.; Zhang, P.; Wu, S.; Li, Y.; Wen, W.; Jiang, Z.; Mi, J.; Zhu, Z.; Yang, Y. *Chem. Mater.* **2013**, *25*, 2014−2020.
(42) Gorlin, Y.; Lassalle-Kaiser, B.; Benck, J. D.; Gul, S.; Webb, S. M.; Yachandra, V. K.; Yano, J.; Jaramillo, T. F. *J. Am. Chem. Soc.* **2013**, *135*, 8525−8534.
(43) Pang, Q.; Liang, X.; Kwok, C. Y.; Nazar, L. F. *J. Electrochem. Soc.* **2015**, *162*, A2567−A2576.
(44) Zhang, Q.; Wang, Y.; Seh, Z. W.; Fu, Z.; Zhang, R.; Cui, Y. *Nano Lett.* **2015**, *15*, 3780−3786.
(45) Jiang, Y.; Ma, X.; Feng, J.; Xiong, S. *J. Mater. Chem. A* **2015**, *3*, 4539−4546.
(46) Yi, Z.; Yuan, L.; Sun, D.; Li, Z.; Wu, C.; Yang, W.; Wen, Y.; Shan, B.; Huang, Y. *J. Mater. Chem. A* **2015**, *3*, 3059−3065.
(47) Liu, Y. X.; Si, L.; Zhou, X. S.; Liu, X.; Xu, Y.; Bao, J. C.; Dai, Z. H. *J. Mater. Chem. A* **2014**, *2*, 17735−17739.
(48) Fang, R.; Zhou, G.; Pei, S.; Li, F.; Cheng, H. M. *Chem. Commun.* **2015**, *51*, 3667−3670.

DOI: 10.1021/acs.nanolett.6b00318
Nano Lett. 2016, 16, 2663−2673